Electron-hole asymmetry, Dirac fermions, and quantum magnetoresistance in $BaMnBi_2$

Lijun Li (黎丽君),[1,*] Kefeng Wang (王克锋),[1,†] D. Graf,[2] Limin Wang (王莉敏),[1,†]
Aifeng Wang (王爱峰),[1] and C. Petrovic[1]

[1]*Condensed Matter Physics and Materials Science Department, Brookhaven National Laboratory, Upton, New York 11973, USA*
[2]*National High Magnetic Field Laboratory, Florida State University, Tallahassee, Florida 32306-4005, USA*

(Received 4 February 2016; published 28 March 2016)

We report two-dimensional quantum transport and Dirac fermions in $BaMnBi_2$ single crystals. $BaMnBi_2$ is a layered bad metal with highly anisotropic conductivity and magnetic order below 290 K. Magnetotransport properties, nonzero Berry phase, small cyclotron mass, and the first-principles band structure calculations indicate the presence of Dirac fermions in Bi square nets. Quantum oscillations in the Hall channel suggest the presence of both electron and hole pockets, whereas Dirac and parabolic states coexist at the Fermi level.

DOI: 10.1103/PhysRevB.93.115141

I. INTRODUCTION

In Dirac materials such as graphene, topological insulators Bi_2Se_3 and Bi_2Te_3, copper oxides, and $BaFe_2As_2$ iron pnictide, the energy spectrum of low-energy electrons can be approximated by the relativistic Dirac equation [1–8]. The effective Hamiltonian is characterized by Pauli matrices and even for nonzero effective mass the eigenstates of the Dirac Hamiltonian are spinor wave functions. One of the most interesting aspects of Dirac fermions is quantum transport phenomena [9–11]. In contrast to the conventional electron gas with parabolic energy dispersion, the distance between the lowest and first LLs of Dirac fermions in a magnetic field is large and the quantum limit where all carriers are condensed to the lowest LL is easily realized in moderate magnetic fields [12–15]. Consequently, quantum Hall effect and large linear magnetoresistance (MR) could be observed.

Besides two-dimensional (2D) electronic states in materials such as graphene and topological insulators, bulk $AMnBi_2$ crystals (A = alkaline earth metals such as Sr or Ca) show quasi-two-dimensional (quasi-2D) quantum transport of Dirac fermions [16–19]. Their crystal structure features alternating layers of Mn-Bi edge-sharing tetrahedra and a Bi square net, separated by a layer of A metals. Square bismuth nets host two-dimensional Dirac dispersion in the bulk band structure [16–21]. The characteristics of the Dirac cone is governed by spin-orbit coupling and local arrangement of A atoms that surround the Bi square net. For A = Sr the degeneracy along the band crossing line is lifted except at the place of anisotropic Dirac cone. This is in contrast to A = Ca, where the energy eigenvalue difference due to perturbation potential created by staggered Ca atomic layers cancels out, resulting in a zero-energy line in momentum space [20,22]. Therefore, the selection of A atoms in $AMnBi_2$ presents an opportunity to tune the contribution of Dirac states at the Fermi level, Dirac cone anisotropy and structure. Here we report quasi-2D quantum transport and Dirac fermions in $BaMnBi_2$. We show compensated nature of electronic transport and the presence of both Dirac-like and trivial carriers at the Fermi level.

II. EXPERIMENT

Single crystals of $BaMnBi_2$ were grown from molten metallic fluxes [23]. X-ray diffraction (XRD) data were obtained by using Cu K_α ($\lambda = 0.154\,18$ nm) radiation of a Rigaku Miniflex powder diffractometer on crushed crystals. Electrical transport, magnetization, and heat capacity measurements were performed in a Quantum Design PPMS and MPMS on cleaved and polished single crystals. Polishing is necessary in order to remove residual bismuth droplets from the surface of as-grown single crystals [Fig. 1(a)]. High-field magnetoresistance (MR) was performed at the National High Magnetic Field Laboratory in the same configuration as the in-plane MR. First principle electronic structure calculations were performed using experimental lattice parameters within the full-potential linearized augmented plane wave (LAPW) method implemented in WIEN2k package [24,25]. The general gradient approximation (GGA) was used for exchange-correlation potential [26]. In the calculation, we adopted the antiferromagnetically stacked magnetic structure of $SrMnBi_2$ [27].

III. RESULTS AND DISCUSSION

The unit cell of $BaMnBi_2$ crystals can be indexed in the I4/mmm space group by RIETICA software [Fig. 1(a)] [28]. The lattice parameters $a = b = 0.4627(8)$ nm and $c = 2.4315(7)$ nm are in agreement with the previously reported values [29]. Hence, $BaMnBi_2$ crystal structure [Fig. 1(b)] features identical space group but somewhat elongated c axis when compared to $SrMnBi_2$. The temperature dependence of in-plane resistivity $\rho_{ab}(T)$ and out-of-plane resistivity $\rho_c(T)$ [Figs. 1(c) and 1(d), respectively] suggest considerable transport anisotropy with $\rho_c(T)/\rho_{ab}(T) \approx 20$. Electrical resistivity implies a bad metal with residual resistivities $\rho_{ab0} \approx 0.57\,\text{m}\Omega\text{cm}$ and $\rho_{c0} \approx 19.36\,\text{m}\Omega\text{cm}$. In both $CaMnBi_2$ and $SrMnBi_2$ $\rho_c(T)$ features a broad maximum below 300 K, usually interpreted as a high-T incoherent to low-T coherent conduction in quasi-2D electronic systems [30,31]. The temperature dependence of c axis resistivity [Fig. 1(d)] suggests that $BaMnBi_2$ $E_F\tau$ values (where E_F is Fermi energy and

*Present address: Key Laboratory of Materials Physics, Institute of Solid State Physics, Chinese Academy of Sciences, Hefei 230031, Peoples Republic of China.
†Present address: Department of Physics, University of Maryland, College Park, MD 20742-4111, USA.

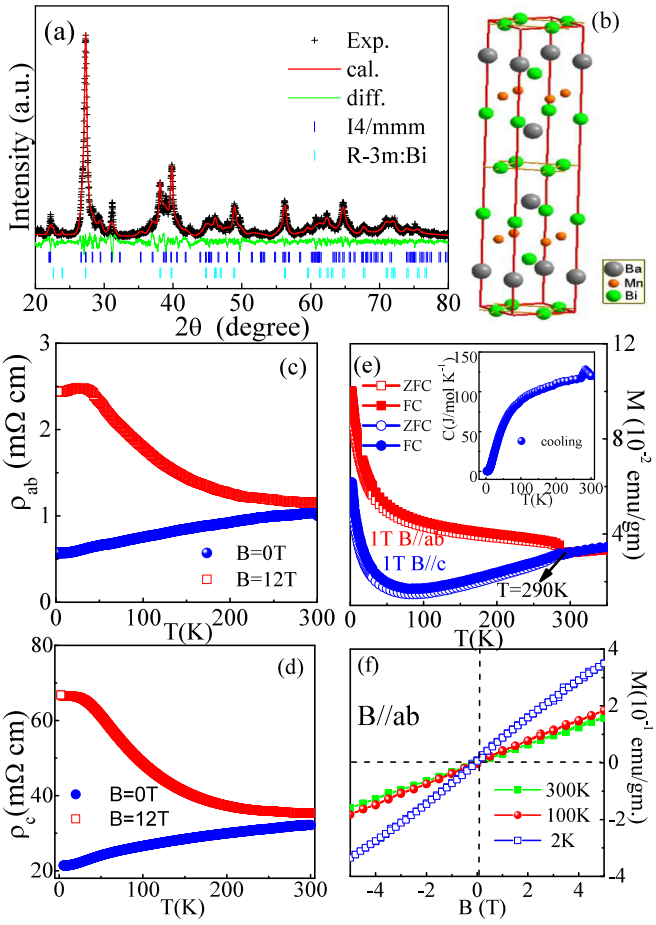

FIG. 1. (a) Powder XRD patterns and refinement results. The data were shown by (+), fitting and difference curves are given by the red and green solid line, respectively. (b) Crystal structure of $BaMnBi_2$. (c, d) Temperature dependence of the in-plane resistivity $\rho_{ab}(T)$ and c-axis resistivity $\rho_c(T)$ of the $BaMnBi_2$ single crystal in the $B = 0$ T (solid symbols) and $B = 12$ T (open symbols) magnetic fields, respectively. (e) Temperature dependence of magnetization $M(T)$ for applied magnetic field parallel and perpendicular to the ab plane in both zero-field-cooling (ZFC, solid symbols) and field-cooling (FC, open symbols). The inset in (e) shows temperature dependence of heat capacity. (f) Magnetization hysteresis loops M(H) of $BaMnBi_2$, at 300 K, 100 K, and 2 K.

τ is the scattering time) are different from $CaMnBi_2$ and $SrMnBi_2$ so that the coherent-incoherent crossover is above 300 K. An external magnetic field $B = 12$ T strongly enhances the resistivity. The MR ratio $MR = [\rho(B) - \rho(0)]/\rho(0)$ exceeds 300% for the in plane MR (MR_{ab}) and 200% for the c-direction MR (MR_c) at 2 K and 12 T. Temperature dependence of the magnetic susceptibility $M(T)$ measured in 1 T is shown in Fig. 1(e). The M-T curves are similar to $SrMnBi_2$ and $CaMnBi_2$ with a magnetic anomaly around 290 K [17,18,21,32]. A clear λ-type peak appears in heat capacity at around $T = 290$ K, whereas the linear specific heat coefficient $C \sim \gamma T$ is obtained to be 34.7(1) mJ mol^{-1} K^{-2} from the specific heat data [Fig. 1(e) inset]. Magnetization hysteresis loops [Fig. 1(f)] also support the antiferromagnetic nature of $T = 290$ K transition.

Figures 2(a) and 2(b) shows field-angular-dependence of the in plane resistivity $\rho_{ab}(B, \theta)$ at $T = 2$ K . When B is

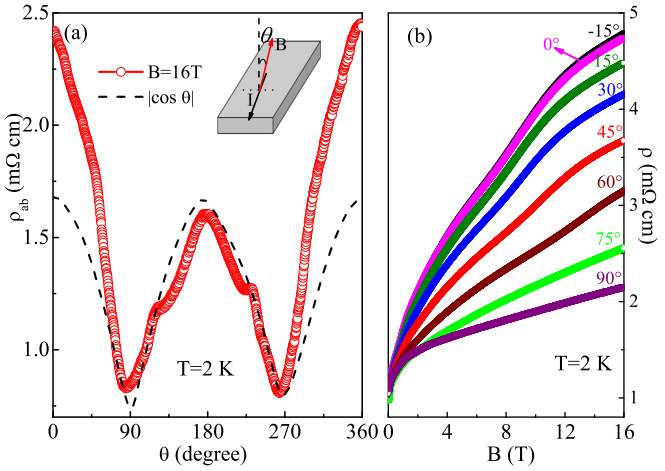

FIG. 2. The crystal was fixed on a rotating stage so that the tilt angle θ between the crystal surface (ab plane) and the magnetic field can be continuously changed and the current is flowing in the ab plane perpendicular to magnetic field. (a) Tilt angle θ (from 0° to 360°) dependence of in-plane resistivity (ρ_{ab}) at $B = 16$ T as $T = 2$ K. The black dash line is the $|\cos(\theta)|$ curve. The inset shows the configuration of the measurement. (b) In-plane resistivity ρ_{ab} vs. magnetic field B at different tilt angles θ at 2 K (−15° to 90°).

parallel to the c axis ($\theta = 0°$, 180°, 360°), the MR is maximized and is linear in field for high fields with the presence of angular-dependent quantum oscillations. With increase in the tilt angle θ, the MR gradually decreases to the minimal value when B is in the ab plane ($\theta = 90°$, 270°). The MR bears close resemblance to the $|\cos(\theta)|$ angular dependence [dashed black line in Fig. 2(a)] observed in $SrMnBi_2$ and $CaMnBi_2$ [16,17], however, with some deviations. This could suggest the presence of 3D, in addition to quasi-2D electronic transport in $BaMnBi_2$.

Large anisotropy can be observed in $BaMnBi_2$ resistivity in magnetic field [Figs. 3(a) and 3(b)] when the current is applied along a and c axes. The inset in Fig. 3(a) shows magnetic field dependence of the $\Delta R_{ab} = R_{ab}$-$\langle R_{ab}\rangle$ curves, where $\langle R_{ab}\rangle$ is a smooth background. With the increase in magnetic field, oscillations appear at fairly low magnetic fields at low temperatures. Magnetic field dependence of Hall magnetoresistance $R_H(B)$ also shows quantum oscillations below 50 K [Fig. 3(c)]. This is clear from the inverse field dependence of $\Delta R_H = R_H$-$\langle R_H\rangle$ [Fig. 3(c) inset]. The oscillating component shows a periodic behavior in $1/B$. Figure 3(d) presents Landau levels (LL) index versus the integer n extracted from quantum oscillations. The absolute value of the intercept of the linear fit yields the Berry phase, expected to be zero for conventional metals and 1/2 for Dirac fermions. The Berry phase and the ∼1/2 intercept of the linear fit of LLs have been observed in Dirac materials, such as monolayer graphene and topological insulators [13]. As shown in Fig. 3(d), the absolute intercept values of R_H and R_{ab} are 0.3 and 0.2, respectively, consistent with possible larger contribution of parabolic bands at the Fermi surface when compared to $SrMnBi_2$ and $CaMnBi_2$ or significant electron-hole asymmetry [16,17,20,33].

The fast Fourier transform (FFT) spectrum of the resistivity oscillations at 1.55 K [Fig. 4(a)] reveals a periodic behavior

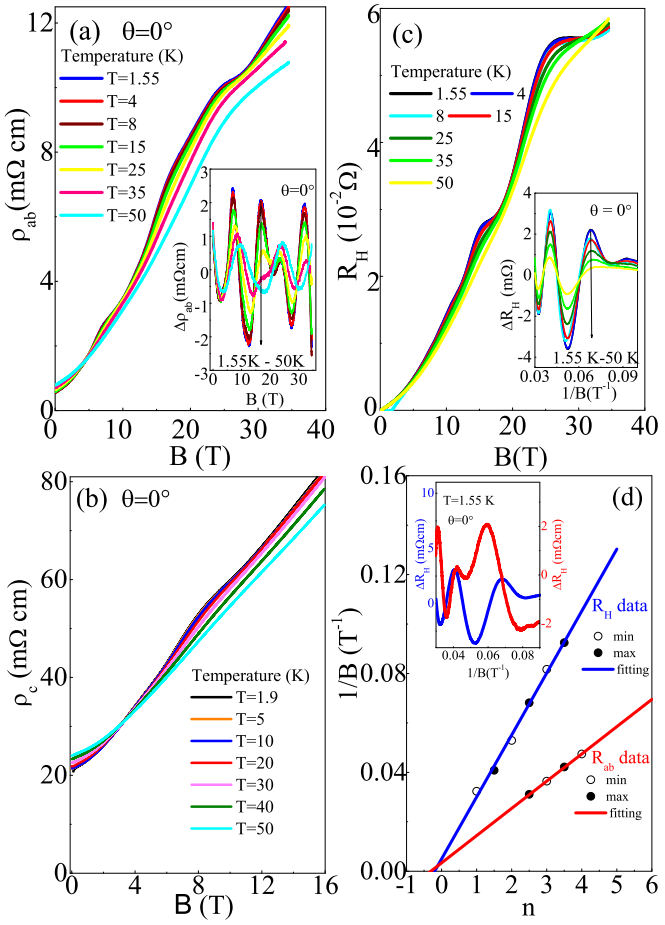

FIG. 3. (a) In plane ρ_{ab}-B and (b) c-axis resistivity ρ_c-B of $BaMnBi_2$ crystal measured at different temperatures. (c) Magnetic field dependence of Hall resistance. (d) The integer Landau levels as a function of inverse field; the arrows indicate the positions of the estimated LL index n labeled by the numbers. Insets in (a) and (c) present magnetoresistant SdH oscillations of $\Delta R_i = R_i - \langle R_i \rangle$ as a function of B where $i = ab, c$.

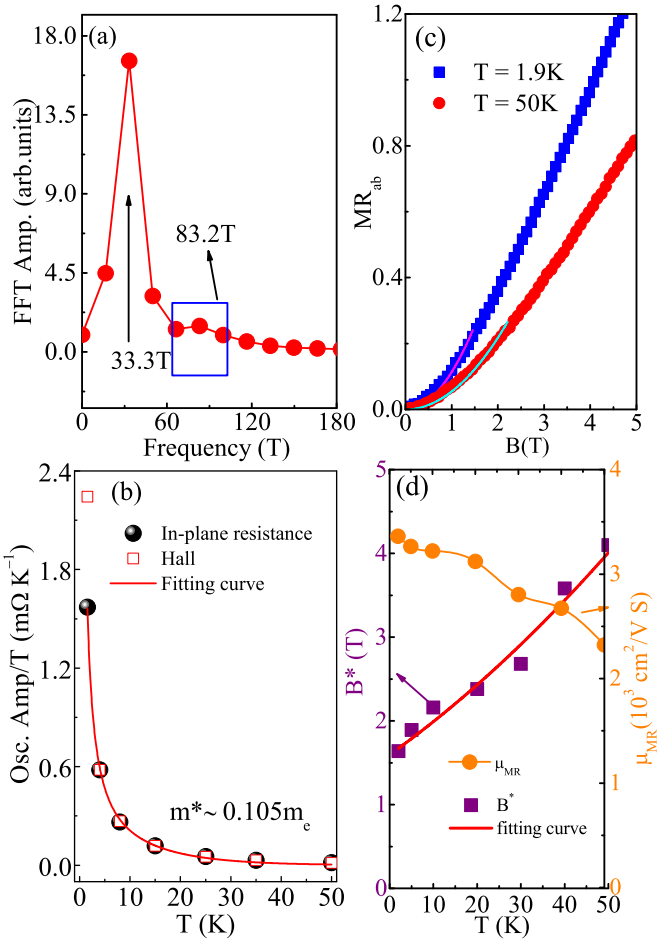

FIG. 4. (a) The Fourier transform spectrum of the SdH oscillation at $T = 1.55$ K. (b) Temperature dependence of the temperature divided oscillation amplitude (Osc.Amp./T-T) in magnetoresistant SdH oscillations, the black balls are obtained from ΔR_{ab} data, and the red squares are obtained from ΔR_H data. The red line is the fitting results giving cyclotron mass $m^* \sim 0.105m_e$. (c) In-plane low-field magnetoresistance (MR_{ab}) for $T = 1.9$ K (blue solid squares) and $T = 50$ K (red solid circles); the lines are fitting results of $MR = A_2 \times B^2$. (d) Temperature dependence of the critical field B^* (purple solid squares) and the effective MR mobility (orange solid circles) μ_{MR} obtained by fitting the low-field MR_{ab}. The red solid line is the fitting results of B^* using $B^* = \frac{1}{2e\hbar v_F^2}(E_F + \kappa_B T)^2$.

in $1/B$, a clear main frequency $F = 33.3$ T, and a possible weakly resolved frequency at 83.2 T. Both are smaller than that of $SrMnBi_2$ ($F = 138$ T) and $CaMnBi_2$ ($F_1 = 101$ T and $F_2 = 181$ T) (Table I) [16,18]. The frequency of main oscillation is related to the Fermi surface averaged Fermi wave vector via the Onsager relation $F = (\hbar c/2\pi e)\pi k_F^2$, giving $k_F = 3.2 \times 10^8$ m^{-1} and the averaged carrier density $n = [2/(2\pi)^3](4\pi/3k_F^3) = 1.10 \times 10^{24}$ m^{-3} [33–35]. The cyclotron effective mass m^* can be obtained by using the Lifshitz-Kosevitch formula [34]: $\Delta R = \frac{2\pi^2\kappa_B m^* T\gamma/eB\hbar}{\sinh(2\pi^2\kappa_B m^* T\gamma/eB\hbar)}$, where $\gamma = 1$ is a constant. Setting $K = \frac{2\pi^2\kappa_B m_e}{e\hbar} \simeq 14.7$ TK^{-1}, $m^* = \mu \times m_e$, B determined by the FFT range: $1/B = (0.03 + 0.09)/2 = 0.06$. So $K/B \simeq 0.8824$. The above formula can be changed into the following simpler form: $\Delta R/T = \frac{0.8824\mu}{\sinh(0.8824T\mu)}$. The fitting result is plotted by using the red line in Fig. 4(b), giving the cyclotron mass $m^* \approx 0.105m_e$, where m_e is the free electron mass. The cyclotron mass m^* of $BaMnBi_2$ is smaller than that of $CaMnBi_2$ with $m^* = 0.35m_e$ and $SrMnBi_2$ with $m^* = 0.29(2)m_e$ as shown in Table I [17,18].

Assuming that cyclotron mass reflects mostly quasi-2D Dirac fermions, we estimate Fermi velocity from $v_F = \hbar k_F/m^* = 3.5 \times 10^5$ m/s, where $m^* = 0.1m_e$. The low magnetic field range of the in-plane magnetoresistance (MR_{ab}) unperturbed by quantum oscillations is shown in Fig. 4(c). The experimental data can be well fitted by using semiclassical model, as $MR \sim A_2B^2$ for $B < 3$T. In a multiband system with both Dirac and conventional parabolic-band carriers (such as electrons and holes), the coefficient of the low-field semiclassical B^2 quadratic term A_2 is related to the effective MR mobility when the Dirac carriers are dominant in transport: $\sqrt{A_2} = \frac{\sqrt{\sigma_e\sigma_h}}{\sigma_e+\sigma_h}(\mu_e + \mu_h) = \mu_{MR}$, where σ_e, σ_h, μ_e, and μ_h are the effective electron and hole conductivity and mobility at zero field, respectively. Figure 4(d) shows the temperature dependence of μ_{MR}. At about 2 K, the value

TABLE I. Parameters for $CaMnBi_2$, $SrMnBi_2$, and $BaMnBi_2$. T_M is the magnetic transition temperature, m^* is the cyclotron mass, F is the frequency obtained by FFT, E_F is the Fermion energy level, v_F is the Fermi velocity, and μ_{MR} is the effective MR mobility.

Compounds	$T_M(K)$	$m^*(m_e)$	$F(T)$	$E_F(meV)$	$v_F(\times 10^5 m/s)$	$\mu_{MR}(2K)(\mathrm{cm}^2/\mathrm{Vs})$	References
$CaMnBi_2$	270	0.35	101, 181	—	—	1800	[17,32]
$SrMnBi_2$	290	0.29(2)	138	4.97	5.13	3400	[16,18,21]
$BaMnBi_2$	290(1)	0.105(1)	33.3(4),83.2(5)	7.37(3)	1.60(8)	3363(1)	This work

of μ_{MR} is $\sim 3360\,\mathrm{cm}^2/\mathrm{Vs}$, similar to $SrMnBi_2$ with μ_{MR} is $\sim 3400\,\mathrm{cm}^2/\mathrm{Vs}$ [16].

Above a characteristic field B^*, as $B > B^*$, MR is nearly linear $MR \sim A_1 B + O(B^2)$, where $O(B^2)$ is very small. The evolution of B^* with temperature is shown in Fig. 4(d). The energy splitting between the lowest and the first LLs of Dirac fermions can be described by $\Delta_{LL} = \pm v_F \sqrt{2eB\hbar}$ (v_F is the Fermi velocity) [13,14]. In the quantum limit at specific temperature and field, Δ_{LL} becomes larger than both the Fermi energy E_F and the thermal fluctuations $\kappa_B T$, so all carriers occupy the lowest Landau level, resulting in linear magnetoresistance [11,12]. The critical field B^* above which the quantum limit is satisfied at a specific temperature T is $B^* = \frac{1}{2e\hbar v_F^2}(E_F + \kappa_B T)^2$ [15]. The temperature dependence of the critical field B^* in $BaMnBi_2$ can be well fitted by the above equation. The fitting [Fig. 5(b)] gives $E_F \approx 7.38$ meV, $v_F \approx 1.61 \times 10^5$ m/s (Table I), in agreement with quantum oscillation measurement. The estimated Fermi velocity is similar to $SrMnBi_2$ [16], confirming the existence of Dirac fermion states in $BaMnBi_2$.

The first principle calculation shows the presence of near-linear energy dispersion and both electron- and hole-like bands near the Fermi level [Fig. 5(a)]. Both Mn- and Bi-derived bands make contributions at the density of states (DOS) near E_F [Figs. 5(b) and 5(c)]. Interestingly, we observe quantum oscillations in the Hall coefficient. Within Boltzmann transport theory, if electronic transport is governed by a single band with single scattering rate, oscillations in ρ_{xy} are not expected since the scattering rate cancels out in the Hall channel. This reveals the compensated nature of electronic transport with both electron and hole pockets at the Fermi surface in $BaMnBi_2$, i.e., at least two types of pockets with different mobility [20,36,37]. The positive sign indicates that the larger (or higher mobility) pocket corresponds to the hole band near Γ point [20].

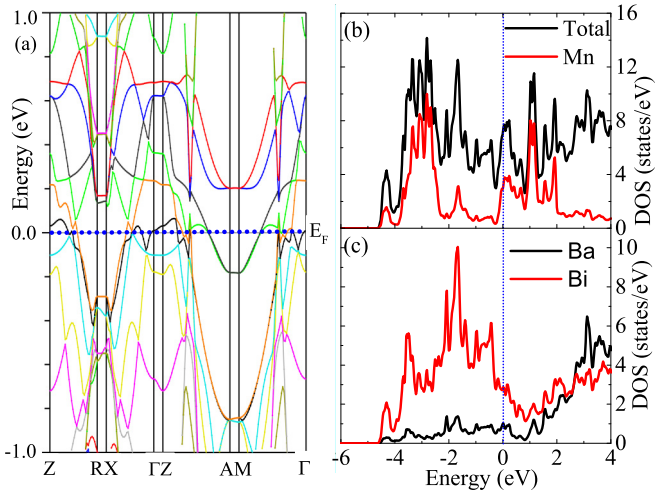

FIG. 5. (a) The band structure for $BaMnBi_2$ with antiferromagnetic order but without spin-orbit coupling. (b, c) The total and local density of states from Mn, Ba, and Bi atoms for AFM $BaMnBi_2$. The dotted line indicates the position of the Fermi energy. In the calculation, the moments of Mn atoms are arranged in an antiferromagnetic order in the ab plane but the Mn layers are ferromagnetically stacked along the c axis.

Compensated nature of electronic transport is similar to not only another Dirac semimetal Cd_3As_2 but also to copper oxides and β-FeSe [38–40]. For $BaMnBi_2$ it indicates the presence of trivial (parabolic-like) electron band in addition to Dirac-like hole band at the Fermi surface [33], in agreement with Fig. 5(a). On the other hand, in $SrMnBi_2$ the electron-hole asymmetry due to spin-orbit coupling is intrinsic property of the anisotropic Dirac cone and therefore Berry phase cannot be quantized to $\beta = \pi$ [20]. This could also influence the intercept value shown in Fig. 4(d) and could contribute to quantum oscillations in the Hall channel.

IV. CONCLUSION

In summary, we demonstrate the quantum transport in $BaMnBi_2$. When compared to other $AMnBi_2$ (A = Ca, Sr, Ba) materials, it can be concluded that alkaline earth atoms have minor influence on the antiferromagnetic transition temperature. Larger A atoms do bring the change of the unit cell space group from P4/nmm (A = Ca) to I4/mmm (A = Sr, Ba). The change of the space group, however, does change stacking of alkaline earth atoms above and below Bi square net from coincident (A = Ca) to staggered (A = Sr, Ba) [20]. Somewhat elongated c axis for A = Ba when compared to A = Sr material results in larger electron-hole asymmetry and deviation from the Berry phase $\beta = \pi$. This agrees with first-principles result that the main factor for the anisotropic Dirac band is the anisotropic potential created by the Sr/Ba atoms [20]. $AMnBi_2$ materials therefore represent a platform to tune the anisotropy of Dirac cone states in the background of magnetic order. To that regard, it would be of interest to study magnetic exchange in $BaMnBi_2$ and its potential coupling to Dirac states [27].

ACKNOWLEDGMENTS

Work at Brookhaven is supported by the U.S. DOE under Contract No. DE-SC0012704. Work at the National High Magnetic Field Laboratory is supported by the NSF Cooperative Agreement No. DMR-0654118, and by the state of Florida.

[1] T. O. Wehling, A. M. Black-Schaffer, and A. V. Balatsky, Adv. Phys. **63**, 1 (2014).

[2] K. S. Novoselov, A. K. Geim, S. V. Morozov, D. Jiang, M. I. Katsnelson, I. V. Grigorieva, S. V. Dubonos, and A. A. Firsov, Nature **438**, 197 (2005).

[3] M. Z. Hasan and C. L. Kane, Rev. Mod. Phys. **82**, 3045 (2010).

[4] X. L. Qi and S. C. Zhang, Rev. Mod. Phys. **83**, 1057 (2011).

[5] J. Orenstein and A. J. Millis, Science **288**, 468 (2000).

[6] P. Richard, K. Nakayama, T. Sato, M. Neupane, Y.-M. Xu, J. H. Bowen, G. F. Chen, J. L. Luo, N. L. Wang, X. Dai, Z. Fang, H. Ding, and T. Takahashi, Phys. Rev. Lett. **104**, 137001 (2010).

[7] A. K. Geim and K. S. Novoselov, Nat. Mater. **6**, 183 (2007).

[8] G. W. Semenoff, Phys. Rev. Lett. **53**, 2449 (1984).

[9] A. H. Castro Neto, F. Guinea, N. M. R. Reres, K. S. Novoselov, and A. K. Geim, Rev. Mod. Phys. **81**, 109 (2009).

[10] Huan Yang, Benoit Fauque, Liam Malone, Arlei B. Antunes, Zengwei Zhu, Citrad Uher, and Kamran Behnia, Nat. Commun. **1**, 47 (2010).

[11] A. A. Abrikosov, Phys. Rev. B **58**, 2788 (1998).

[12] A. A. Abrikosov, *Fundamentals of the Theory of Metals* (North-Holland, Amsterdam, 1988).

[13] Y. Zhang, Z. Jiang, Y.-W. Tan, H. L. Stormer, and P. Kim, Nature (London) **438**, 201 (2005).

[14] D. Miller, K. Kubista, G. Rutter, M. Ruan, W. de Heer, P. First, and J. Stroscio, Science **324**, 924 (2009).

[15] K. K. Huynh, Y. Tanabe, and K. Tanigaki, Phys. Rev. Lett. **106**, 217004 (2011).

[16] K. Wang, D. Graf, H. Lei, S. W. Tozer, and C. Petrovic, Phys. Rev. B **84**, 220401(R) (2011).

[17] Kefeng Wang, D. Graf, Limin Wang, Hechang Lei, S. W. Tozer, and C. Petrovic, Phys. Rev. B **85**, 041101(R) (2012).

[18] J. Park, G. Lee, F. Wolff-Fabris, Y. Y. Koh, M. J. Eom, Y. K. Kim, M. A. Farhan, Y. J. Jo, C. Kim, J. H. Shim, and J. S. Kim, Phys. Rev. Lett. **107**, 126402 (2011).

[19] L.-L. Jia, Z.-H. Liu, Y.-P. Cai, T. Qian, X.-P. Wang, H. Miao, P. Richard, Y.-G. Zhao, Y. Li, D.-M. Wang, J.-B. He, M. Shi, G.-F. Chen, H. Ding, and S.-C. Wang, Phys. Rev. B **90**, 035133 (2014).

[20] G. Lee, M. A. Farhan, J. S. Kim, and J. H. Shim, Phys. Rev. B **87**, 245104 (2013).

[21] J. K. Wang, L. L. Zhao, Q. Yin, G. Kotliar, M. S. Kim, M. C. Aronson, and E. Morosan, Phys. Rev. B **84**, 064428 (2011).

[22] Ya Feng, Zhijun Wang, Chaoyu Chen, Yoguo Shi, Zhuojin Xie, Hemian Yi, Aiji Liang, Shaolong He, Junfeng He, Yingying Peng, Xu Liu, Yan Liu, Lin Zhao, Guodong Liu, Xiaoli Dong, Jun Zhang, Chuangtian Chen, Zuyan Xu, Xi Dai, Zhong Fang, and X. J. Zhou, Sci. Rep. **4**, 5385 (2014).

[23] Z. Fisk and J. P. Remeika, in *Handbook on the Physics and Chemistry of Rare Earths*, edited by K. A. Gschneidner Jr. and L. Eyring (Elsevier, Amsterdam, 1989), Vol. 12, Chap. 81, pp. 53–70.

[24] M. Weinert, E. Wimmer, and A. J. Freeman, Phys. Rev. B **26**, 4571 (1982).

[25] P. Blaha, K. Schwartz, G. K. H. Madsen, D. Kvasnicka, and J. Luitz, *WIEN2K, An Augmented Plane Wave and Local Orbitals Program for Calculating Crystal Properties* (Karlheinz Scharz, Techn. Universität Wien, Austria), 2001.

[26] J. P. Perdew, K. Burke, and M. Ernzerhof, Phys. Rev. Lett. **77**, 3865 (1996).

[27] Y. F. Guo, A. J. Princep, X. Zhang, P. Manuel, D. Khalyavin, I. I. Mazin, Y. G. Shi, and A. T. Boothroyd, Phys. Rev. B **90**, 075120 (2014).

[28] B. Hunter, RIETICA-A Visual RIETVELD Program, International Union of Crystallography Commission on Powder Diffraction Newsletter No. 20 (Summer) (1998) [http://www.rietica.org].

[29] G. Cordier and H. Schäfer, Zeitschrift für Naturforschung B **32**, 383 (1977).

[30] D. B. Gutman and D. L. Maslov, Phys. Rev. Lett. **99**, 196602 (2007).

[31] D. B. Gutman and D. L. Maslov, Phys. Rev. B **77**, 035115 (2008).

[32] J. B. He, D. M. Wang, and G. F. Chen, Appl. Phys. Lett. **100**, 112405 (2012).

[33] Yoichi Ando, J. Phys. Soc. Jpn. **82**, 102001 (2013).

[34] D. Shoeneberg, *Magnetic Oscillation in Metals* (Cambridge University Press, Cambridge, UK, 1984).

[35] K. Eto, Z. Ren, A. A. Taskin, K. Segawa, and Y. Ando, Phys. Rev. B **81**, 195309 (2010).

[36] N. Kikugawa, A. W. Rost, C. W. Hicks, A. J. Schofield, and A. P. Mackenzie, J. Phys. Soc. Jpn. **79**, 024704 (2010).

[37] S. Chakravarty and Hae-Young Kee, Proc. Natl. Acad. Sci. **105**, 8835 (2008).

[38] L. P. He, X. C. Hong, J. K. Dong, J. Pan, Z. Zhang, J. Zhang, and S. Y. Li, Phys. Rev. Lett. **113**, 246402 (2014).

[39] N. Doiron-Leyraud, C. Proust, D. LeBoeuf, J. Levallois, J. B. Bonnemaison, R. Liang, D. A. Bonn, W. N. Hardy, and L. Taillefer, Nature (London) **447**, 565 (2007).

[40] M. D. Watson, T. Yamashita, S. Kasahara, W. Knafo, M. Nardone, J. Beard, F. Hardy, A. McCollam, A. Narayanan, S. F. Blake, T. Wolf, A. A. Haghighirad, C. Meingast, A. J. Schofield, H. v. Löhneysen, Y. Matsuda, A. I. Coldea, and T. Shibauchi, Phys. Rev. Lett. **115**, 027006 (2015).